Experimental and numerical analysis of micromechanical damage in the punching process for High-Strength Low-Alloy steels

Mohamed Achouri [a,b,*], Guenael Germain [a], Philippe Dal Santo [a], Delphine Saidane [b]

[a] LAMPA Laboratory (EA 1427), Arts et Métiers ParisTech, 2 Bd du Ronceray, 49000 Angers, France
[b] DEVILLE ASC, ZI de Beauregard, 49150 Baugé, France

Keywords:
Punching
Damage
Fracture initiation
Micro-voids
Numerical simulation
Stress state

A B S T R A C T

Sequential sheet metal forming processes can result in the accumulation of work hardening and damage effects in the workpiece material. The mechanical strength of the final component depends on the "evolution" of these two characteristics in the different production steps. The punching process, which is usually in the beginning of the production chain, has an important impact on the stress, strain and damage states in the punched zones. It is essential that the influence of these mechanical fields be taken into account in the simulation of the forming sequence. In order to evaluate the evolution of each phenomenon, and in particular damage accumulation in the forming process, it is essential to characterize the punching process. The objective of this work is to understand and identify the physical damage mechanisms that occur during the punching operation and to establish relevant numerical models to predict the fracture location. The effect of the punch–die clearance on mechanical fields distribution is also discussed in this work.

1. Introduction

Punching is one of the most commonly used industrial sheet metal forming processes. It allows the elaboration of components using a relative small number of passes. The punching process is generally followed by other forming processes such as bending, edge rounding, stamping, and hydro-forming. The performance of these subsequent operations is thus related to the punching operation and the strain history in the punched zones. It is therefore important to identify and characterize the behavior and evolution of the damage caused by punching in order to take into account these phenomena in the global formability analysis of the manufacturing cycle. Good understanding of the damage mechanisms involved during shearing can reduce and limit damage, via the good management of the complete set of forming process parameters.

In the punching process, damage appears gradually in the sheet metal following the onset of plastic deformation and corresponds to a drop of the punching force. In terms of the numerical simulation of punching, there are two principal approaches: (a) empirical models and (b) models based on the evolution of a damage parameter. The first approach does not consider damage variables. A function of the loading and strain histories is used. This function is assumed to be capable of indicating the damage level. Hambli and Potiron [1] and Lemiale et al. [2] have published reviews of these criteria. Several criteria have been studied, including the Cockcroft–Latham criterion [3], the Rice and Tracey criterion [4] and the Oyane criterion [5]. This author has determined the critical value for each criterion by knowing the punch penetration value at rupture and by adjusting the effect of the clearance between the punch and the die. The author proposed a modification of the Rice and Tracey criterion. This modification was justified by its ability to predict the penetration at fracture in relation to the influence of the clearance between the punch and the die.

Other studies have shown that the Cockroft–Latham criterion is able to realistically predict the penetration at failure [6–11]. Bacha et al. [10] showed that in the zone between the punch and the die, large deformations are localized prior to the initiation and propagation of cracks. The crack path is controlled by the stress and strain fields in this area and the damage parameter is based on the accumulated plastic strain. These models, in which the damage is not coupled to the plasticity, have the advantage of being simple to implement in finite element codes and have a small number of parameters to identify. However, it has been shown experimentally that they overestimate the punching loads and are not capable of predicting the damage for complex loading paths and large plastic strain, which is the case for the punching process ([6,11–16]).

The second family of models is based on a coupled approach. In this category two damage models are widely used in metal

* Corresponding author at: LAMPA Laboratory (EA 1427), Arts et Métiers ParisTech, 2 Bd du Ronceray, 49000 Angers, France. Tel.: +33 647397990.
E-mail address: mohamed.achouri@ensam.eu (M. Achouri).

punching. The first was proposed by Lemaitre [17] and is based on the thermodynamics of irreversible processes. The concepts of effective stress and strain equivalence are used to makes it possible to define a damage variable. The second model was proposed by Gurson, [18] Tvergaard and Needleman GTN [19] and is based on the analysis of the evolution of micro-cavities (nucleation, growth and coalescence). This model has the advantage of describing the physical evolution of the failure mechanisms. However, it is limited by the fact that shear effects are not taken into account in its formulation. This makes the model unable to predict damage localization and fracture under stress states characterized by low stress triaxiality such as those found in the punching process. For conditions in which shear loads are dominate the distortion of ligaments between voids and cavities plays a crucial role in the evolution of the internal degradation of the material. Therefore, to improve the predictive ability of GTN model under low levels of stress triaxiality, Nahshon and Hutchinson [20] and Nielsen and Tvergaard [21] proposed the introduction of a shear mechanism in the evolution law of the cavities.

The objective of this work is to experimentally and numerically characterize the punching process. The study begins with a microscopic analysis to identify the physical damage mechanisms that occur during punching operations, followed by a description of the experimentally observed phenomena using an improved numerical formulation based on a micromechanical approach. The damage predictions using this approach are compared to a non-coupled criterion based on the accumulation of plastic strain as a function of the stress state. Four values of the clearance between the punch and die have been studied in order to validate the predictive capacity of the models investigated in terms of the penetration at fracture initiation and the size of the different zones on the punched profile.

2. Experimental study

2.1. Tooling and operating conditions

Punching tests were carried out using a tool mounted on a hydraulic press (type: MIB) with a capacity of 100 tons, equipped with force and displacement transducers. The tooling consists of a punch and a die with a cylindrical shape (see Fig. 1).

Four punches with four different diameters D_p were used to vary the clearance between the punch and the die.

The normalized clearance is calculated as a percentage of the sheet thickness t by the following equation:

$$J(\%) = \frac{D_d - D_p}{2t} 100 \quad (1)$$

where $\boldsymbol{D_d}$ is the die diameter and $\boldsymbol{D_p}$ is the punch diameter.

The test specimens are square in shape (90×90 mm^2) and are all taken from the same batch of material (thickness $t = 3.55$ mm). Table 1 summarizes the geometry of the punches used. The die diameter is held constant at $D_d = 40.6$ mm. The radii of the cutting edges of the punch and the die are equal to 0.01 mm. All of the tooling (punches and die) is heat-treated to obtain an average hardness of approximately 60 HRC. The hardness of the sheet is approximately 30 HRC. A load cell of type FGS (Fine Guidance Sensor, reference: FN-2554) with a maximum capacity of 50 tons is embedded in the load train to directly measure the applied force (F). The punch displacement (d) is measured by a displacement transducer (type: BALLUFF 02F9-BTL). Both transducers are connected to a data acquisition system. The banking speed is fixed at 300 mm/min.

2.2. Punched profile characterization

In order to characterize the quality of the profile after punching, thirty specimens were prepared for micrographic analysis. Fig. 2 shows the geometry of the parts obtained after the punching operation. The parts were carefully cut at their mid-width (i.e. l/2 width = 45 mm) to analyze the punched profile along the XY plane (zone 1) and YZ plane (zone 2).

The quality of the punched profile is characterized by the width of the following zones:

- The rollover zone: $\boldsymbol{\Delta_{Rol}}$.
- The shear zone: $\boldsymbol{\Delta_{She}}$.
- The fracture zone: $\boldsymbol{\Delta_{Fra}}$.
- The burr zone: $\boldsymbol{\Delta_{bur}}$.
- The fracture angle: $\boldsymbol{\beta_{Fra}}$.

Figs. 3 and 4 show the different areas on the punched edge observed for $J(\%) = 13$.

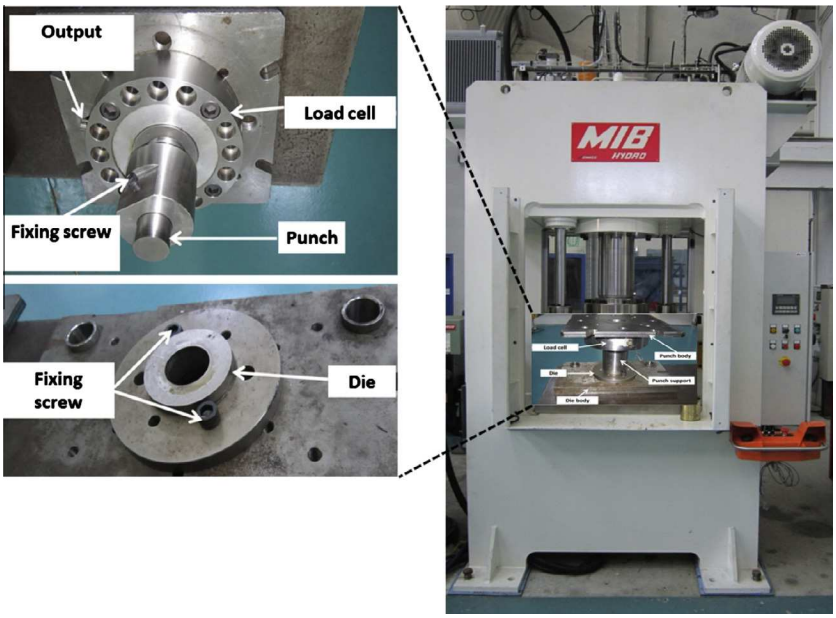

Fig. 1. Punching tools [25].

Table 1
Conditions of punching process.

Condition	Punch diameter D_p (mm)	Clearance J (%)
1	40,12	7
2	39,70	13
3	39,34	17
4	38,36	31

3. Finite element modeling

3.1. Numerical conditions

The commercial finite element package, ABAQUS/Explicit, was used to simulate the punching process as a 2D axisymmetric model. The numerical simulation conditions and the initial mesh are shown in Fig. 5. The size of the elements in the shear zone is 100×100 µm. Axisymmetric 4-node quadratic elements with reduced integration (CAX4R) are used. The Coulomb friction model is used to represent the contact between the sheet and the tools with a coefficient of friction equal to 0.1. The punch and the die are considered to be rigid bodies. The ALE option (Arbitrary Lagrangian Euleurian) [22] is activated to avoid the distortion of elements in the most solicited area [23]. The following three damage models are investigated to determine their predictive capacity in terms of the punching process:

- The classical Gurson–Tvergaard–Needleman model (GTN).
- The modified Gurson–Tvergaard–Needleman for shear loading.
- The ductile fracture initiation criterion.

3.2. The constitutive equations

3.2.1. The Gurson–Tvergaard–Needleman model

In 1977, Gurson [18] deduced a flow potential for the growth of spherical voids. This model is widely-used to describe the evolution of micromechanical damage in ductile materials. In 1984, Tvergaard and Needleman [19] extended the Gurson model by introducing two additional material parameters (q_1 and q_2) to help the model agree better with experiments.

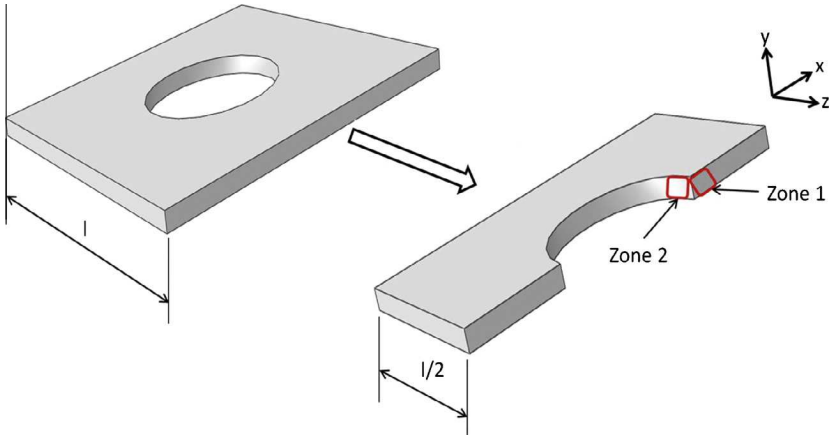

Fig. 2. Preparation of specimens for microscopic analyses.

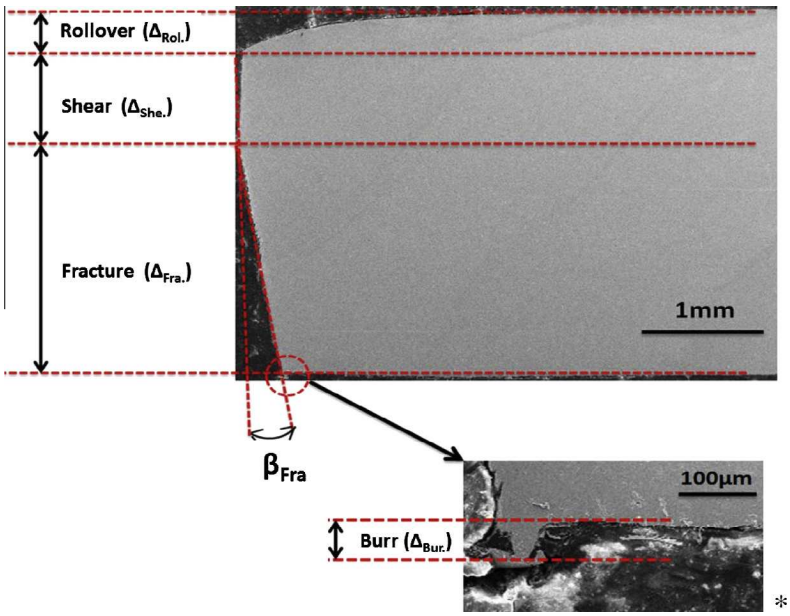

Fig. 3. Experimental punched profile of a component obtained by SEM in zone 1.

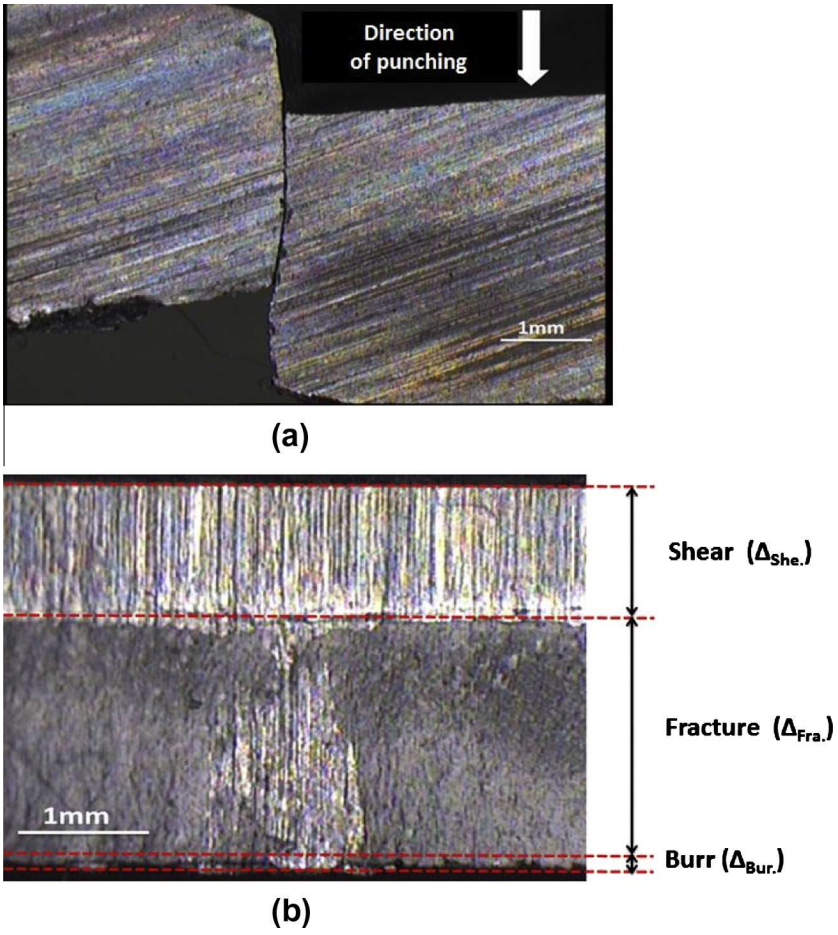

Fig. 4. Punched surface obtained by binocular microscope: (a) in zone 2, (b) in zone 1.

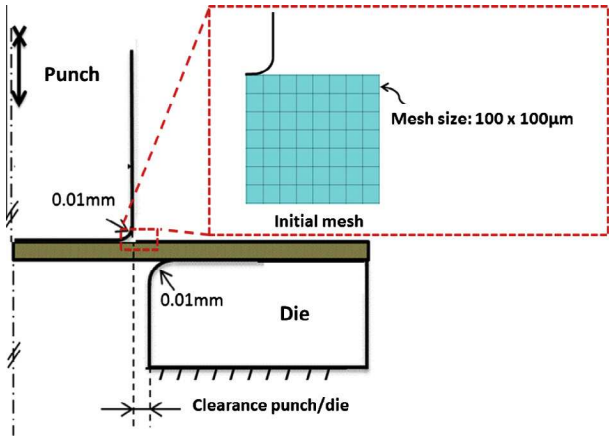

Fig. 5. The boundary conditions and the initial mesh used in the finite element simulations [25].

The flow potential proposed by Gurson–Tvergaard–Needleman (GTN) can be written as:

$$\Phi = \left(\frac{q}{\sigma_0}\right)^2 + 2q_1 f^* \cosh\left(-\frac{3q_2 p}{2\sigma_0}\right) - (1 + q_1^2 f^{*2}) = 0 \tag{2}$$

where σ_0 is flow stress in the fully dense patrix, $q = \sqrt{(3/2)s : s}$ is the von Mises equivalent stress, s is the deviatoric stress tensor and $p = -trace(\sigma)/3$ is the hydrostatic stress.

The damage variable f^*, which takes into account the final decrease in load, is a function of the void volume fraction f:

$$f^* = \begin{cases} f & for\ f \leqslant f_c \\ f_c + (f - f_c)\frac{f_u - f_c}{f_f - f_c} & for\ f > f_c \end{cases} \tag{3}$$

f_c is the critical value of the void volume fraction, $f_u = 1/q_1$ is the ultimate void volume fraction and f_f is the void volume fraction at fracture.

The evolution of the total void volume fraction, due to the plastic strain, is corresponding to the void growth and the nucleation of new voids:

$$\dot{f} = \dot{f}_{growth} + \dot{f}_{nucleation} \tag{4}$$

The increment of volume fraction caused by the void growth is controlled by the trace of plastic strain rate, and takes the following form:

$$\dot{f}_{growth} = (1 - f)tr(\dot{\varepsilon}^p) \tag{5}$$

$\dot{\varepsilon}^p$ is the plastic strain rate tensor.

Assuming the plastic strain only controls the nucleation mechanism as results of inclusions debonding and cracking. The increment of volume fraction caused by the void nucleation, which is controlled by the equivalent plastic strain rate $\dot{\bar{\varepsilon}}^p$, can be written as:

$$\dot{f}_{nucleation} = A\dot{\bar{\varepsilon}}^p \tag{6}$$

Table 2
Parameters of the shear modified Gurson model [25].

Parameters	f_0	q_1	q_2	S_N	f_N	ε_N	f_c	f_f	k_w	η_1	η_2
Values	0.0015	1.2	0.8	0.1	0.02	0.2	0.08	0.13	0.86	0.34	0.7

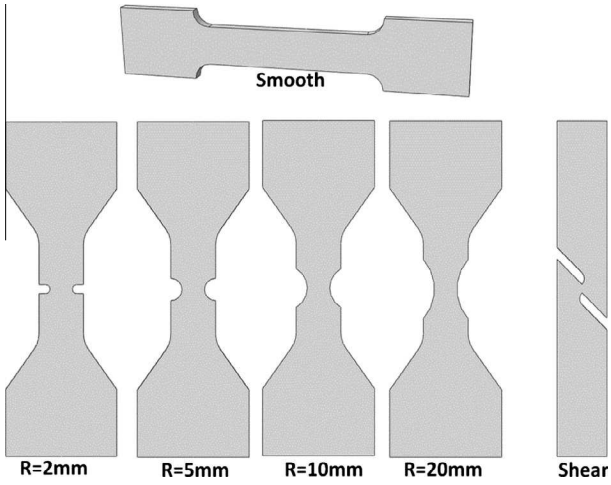

Fig. 6. Different specimen shapes used to characterize the stress state [25].

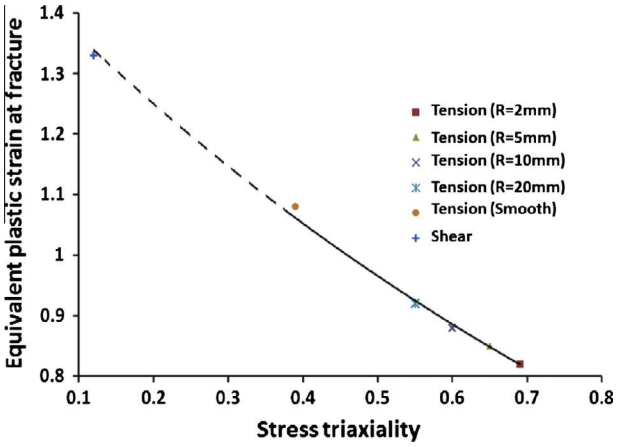

Fig. 7. Evolution of the equivalent plastic strain at fracture versus the stress triaxiality.

The parameter A is defined as a function of the equivalent plastic strain. Chu and Needleman [24] proposed the form of the coefficient A as:

$$A = \begin{cases} \frac{f_N}{S_N\sqrt{2\pi}} \exp\left[-\frac{1}{2}\left(\frac{\bar{\varepsilon}^p - \varepsilon_N}{S_N}\right)^2\right] & \text{for } p \geqslant 0 \\ 0 & \text{for } p < 0 \end{cases} \tag{7}$$

where f_N is the quantity of voids nucleated per unit volume, ε_N is the nucleation strain and S_N is corresponding standard deviation.

3.2.2. Modified GTN model in shear loading

For low stress triaxiality ($\eta = -p/q$), the Gurson model is unable to predict the void growth rate. This issue is the subject of a recent modification of the GTN model, proposed by Nahshon and Hutchinson [20]. This modification introduces a phenomenological term that models the distortion and reorientation of voids dominated by shear stresses. This phenomenon was observed and discussed in [25].

The new expression introduced by Nahshon and Hutchinson [20] is:

$$\dot{f}_{shear} = k_w \frac{f w_0(\boldsymbol{\sigma})}{q} \boldsymbol{s} : \dot{\varepsilon}^p \tag{8}$$

where $w_0(\boldsymbol{\sigma})$ is a function of the stress state, characterized by the normalized third invariant of the deviatoric stress tensor ($\xi = 27J_3/2q^3$). The function $w_0(\sigma)$ is given by:

$$w_0(\sigma) = w_{(\xi)} = 1 - (\xi)^2 \tag{9}$$

where $J_3 = det(s)$ is the third invariant of the deviatoric stress tensor, $\boldsymbol{s} = \boldsymbol{\sigma} + p\boldsymbol{I}$, I is the unit tensor.

The parameter k_w in Eq. (8) is the magnitude of the damage growth rate in shear.

The shear extension in Eqs. (8) and (9) has an important effect in some cases with higher stress triaxiality, like the case of uniaxial tension in a state of plane strain, where the stress triaxiality is approximately 0.577. Nielsen and Tvergaard [21] have introduced a simple extension to improve the damage development prediction at moderate to high stress triaxiality.

The extension has been proposed by introducing an additional factor, $\Omega(\eta)$, in the shear damage evolution term, which depends on the level of stress triaxiality. For this, $w_0(\sigma)$ is expressed in the following form:

$$w_0(\boldsymbol{\sigma}) = w(\boldsymbol{\xi})\Omega(\eta), \text{ with } \Omega(\eta) = \begin{cases} 1, & \text{for } \eta < \eta_1 \\ \frac{\eta - \eta_1}{\eta_1 - \eta_2}, & \text{for } \eta_1 \leqslant \eta \leqslant \eta_2 \\ 0, & \text{for } \eta > \eta_2 \end{cases} \tag{10}$$

where $\eta_1 < \eta_2$ and $w(\xi)$ are given by Eq. (9). This implies that the Hutchinson and Nahshon model is used for $\eta \leqslant \eta_1$, while the GTN model is used for $\eta \geqslant \eta_2$.

Finally, after the addition of the new contribution for shear loads, $\dot{f}_{shear}$, the evolution of the total void volume fraction becomes:

$$\dot{f} = (1-f)tr(\dot{\varepsilon}^p) + A\dot{\bar{\varepsilon}}^p + k_w \frac{f w(\sigma)}{q} s : \dot{\varepsilon}^p \tag{11}$$

This improved Gurson model for shear loading conditions has been implemented in the ABAQUS/Explicit finite element code, using a VUMAT subroutine [26].

The material parameters have been calibrated using an identification strategy based on an experimental campaign using uniaxial tensile tests on smooth, notched and shear specimens, that covers a wide range of stress states. An inverse method is then used to identify the parameters, via comparison between the experimental and numerical data. The Ref. [25] presents more details for the parameters calibration procedure. The material parameters are summarized in Table 2.

3.2.3. Ductile fracture initiation criterion

Ductile fracture predictions in the manufacturing phase can be obtained by the use of a ductile fracture initiation criterion [27]:

$$W = \int_0^{\bar{\varepsilon}_r} \frac{d\bar{\varepsilon}^p}{\bar{\varepsilon}_r(\eta)} = 1 \tag{12}$$

where $\bar{\varepsilon}^p$ is the equivalent plastic strain, $\bar{\varepsilon}_r$ is the plastic strain at fracture and η is the stress triaxiality.

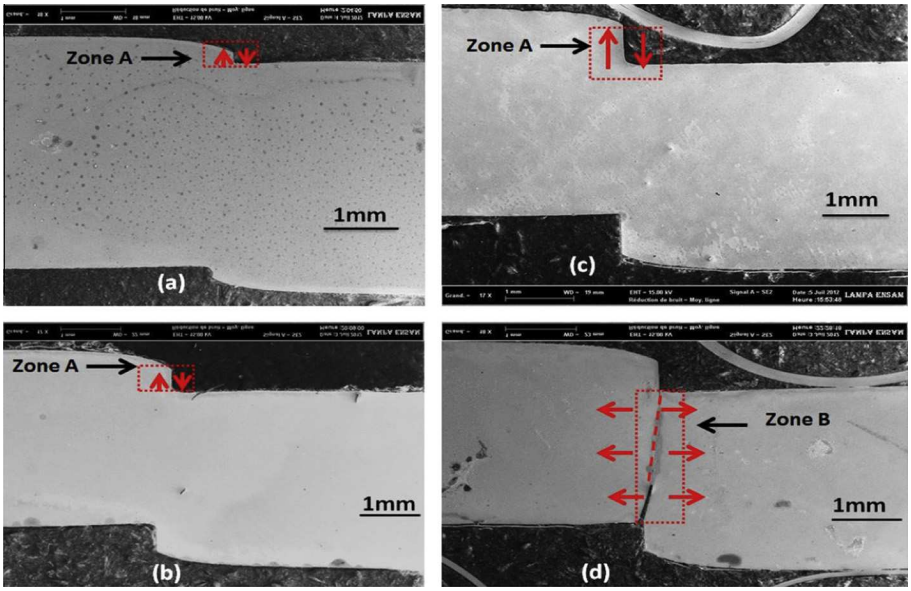

Fig. 8. Macroscopic crack process a function of the punch penetration for $J(\%) = 13$: (a) 12% penetration, (b) 18% penetration, (c) 26.5% penetration and (d) 27.5% penetration.

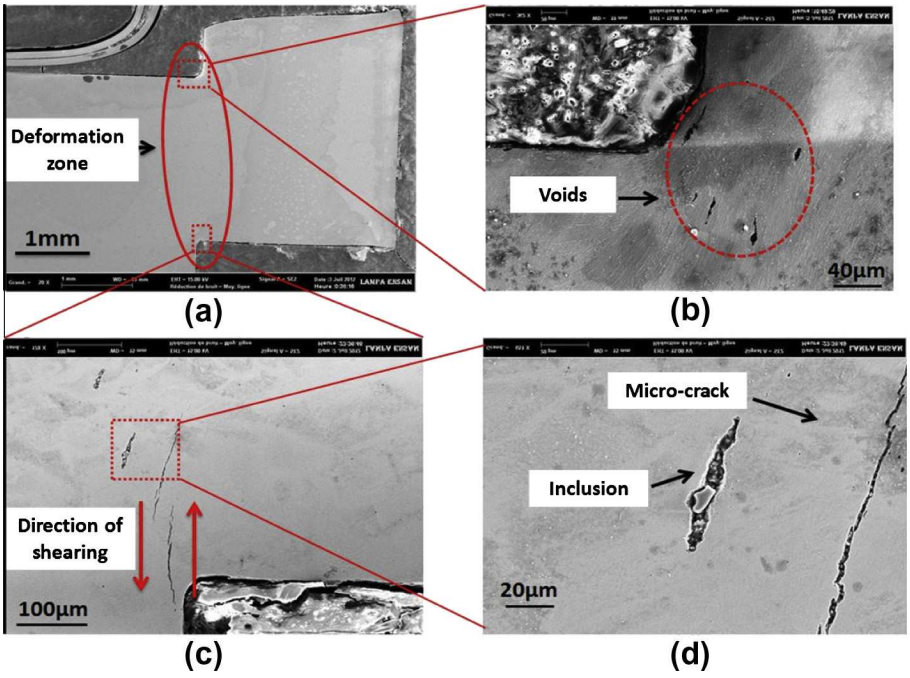

Fig. 9. Microscopic mechanisms for crack creation at 26.5% punch penetration.

Tensile tests using different specimen geometries (see Fig. 6) were carried out to determine the function $\bar{\varepsilon}_r(\eta)$ for different stress states.

The evolution of the stress triaxiality η is calculated numerically at the integration point of the element in which fracture initiation is predicted. The equivalent plastic strain at fracture $\bar{\varepsilon}_r$ corresponds to the drop in load or stress observed in tensile curves. It should be noted that the values of the parameter η are not constant during deformation. Consequently, average values are used to characterize their influence on ductile fracture. The average triaxiality η_{moy} is defined by the following formula [28–31]:

$$\eta = \frac{1}{\bar{\varepsilon}_r}\int_0^{\bar{\varepsilon}_r} \eta d\bar{\varepsilon}^p \tag{13}$$

Fig. 7 shows the evolution of the equivalent plastic strain at fracture as a function of the stress triaxiality which can be expressed in the following exponential form:

$$\bar{\varepsilon}_r(\eta) = 1.48e^{-0.86\eta} \tag{14}$$

In manufacturing processes, where ductile rupture is preceded by a high level of plastic strain, the indicator W can be used to estimate ductile fracture initiation. It is assumed that the fracture

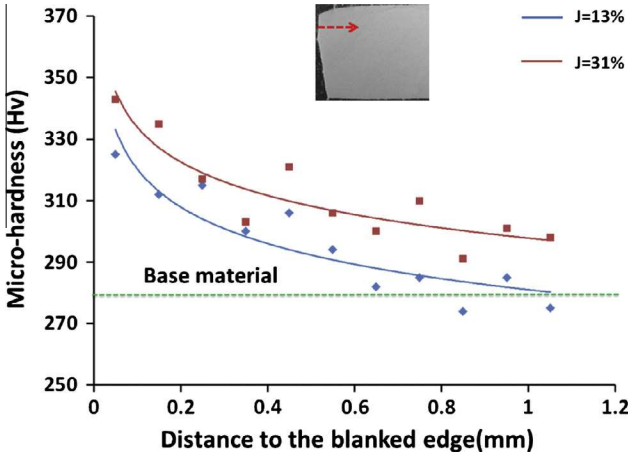

Fig. 10. Micro-hardness profile near the shear zone of the punched surface.

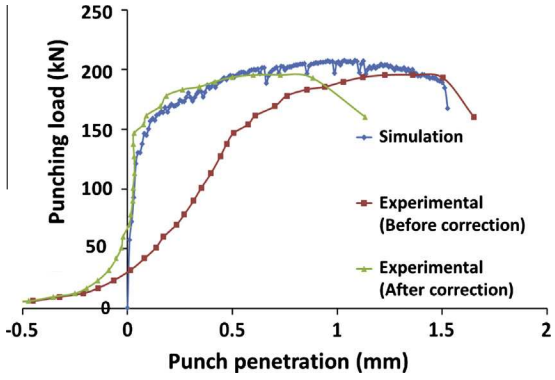

Fig. 11. Correction of the press stiffness.

starts for $W \geqslant 1$. The elements, for which the indicator reaches the critical value, are deleted (using the "kill element" method).

4. Results and discussion

4.1. Experimental results

4.1.1. The process of crack creation

In order to describe the behavior of the sheet metal during the punching process, interrupted tests at various levels of punch penetration have been performed with a clearance of 13%. The specimens were analyzed by SEM (Scanning Electron Microscopy) in order to better understand the mechanisms of deformation and fracture in zone 1 (see Fig. 2) where the plastic strain and damage are located. Selected images from these observations are shown in Fig. 8.

The crack path can be divided into two zones. A smooth area where a shoulder appears on the sheet surface, represented by zone A (Fig. 8a–c), which begins to form parallel to the punching direction. The crack forms under a mode II loading condition (i.e. shear loads). In the area around the tip of the crack (zone B, Fig. 8d), the crack propagates in mode I (i.e. under tensile loads) via deviation from the shear zone to the angle of fracture, β_{rup}. Broberg [32] showed that the damage is limited to a small region at the crack tip. In the next section, the propagation mechanisms in this region are analyzed in detail.

4.1.2. Microscopic crack propagation mechanisms

Fig. 9 shows images obtained just before crack initiation in the zone where the cutting tool edges make contact with the sheet metal for a clearance of 13%. A deformation area is located between the cutting edges of the punch and the die (Fig. 9a). This area is associated with the concentration of the stress, strain, and damage fields. A network of micro-cracks (Fig. 9c and d) with an average size of 150 μm and micro-cavities around inclusions with an average size of 60 μm, is propagated along the shear direction (punching direction). This set of micro-cracks and cavities appears prior to the initiation of the macroscopic crack (zone B in Fig. 8d) which begins by forming the crack-tip via coalescence between multiple defects (voids and micro-cracks). These interactions allow the propagation of the crack-tip to defects created by the contact of the sheet with the cutting edge of the punch (Fig. 9b). The propagation of this network between cavities and micro-cracks leads to the creation of the fracture zone defined by the parameters Δ_{fra} and β_{fra}.

The principal observed results from micrographic analysis are:

- The crack propagates in a deformation zone where the material is completely plastically deformed.
- The damage is limited to the crack-tip which is formed on the cutting edge side of the die to form the fracture zone and that represents fracture initiation.
- The crack propagation mechanisms are defined by the interaction between the cavities and/or micro-cracks. These mechanisms affect locally the crack path.

Also, the crack path is not controlled by the local microstructure of the material, but by the plastic strain field close to the crack-tip.

4.1.3. Impact of the process on the hardness in the vicinity of the punched edge

A series of micro-hardness tests (200 g) were performed on punched specimens for the conditions $J(\%) = 13$ and $J(\%) = 31$. The punched profiles of the specimens used to measure the micro-hardness are similar to those shown in Fig. 3. The aim of these measures is to estimate the evolution of work hardening along the shear zone. Fig. 10 shows that the hardness decreases from the edge of the specimen to its heard. The material hardness is affected by the punching operation over a distance which depends of the punch–die clearance (i.e. about 950 μm for $J(\%) = 13$ and greater than 1 mm for $J(\%) = 31$). For a fixed distance from the edge, the hardness, which reflects the hardening, is higher for a larger clearance.

4.2. Analysis of load–penetration curves

In this section, the experimentally determined load curves, obtained during punching tests, are compared to numerical results.

4.2.1. Press stiffness

Fig. 11 shows a significant difference between the slope of the elastic part of the experimental[1] and numerical curves, for the $J = 13\%$ condition. This difference is related to the stiffness of the press K_{press}, which must be taken into account by correcting the experimental curve. This correction is discussed below and is similar to the method used in Refs. [33,34].

The corrected displacement is given by:

$$\Delta X_{corrected} = \Delta X_{measured} - \Delta X_{press} \tag{15}$$

where:

$$\Delta X_{press} = \frac{F}{K_{press}} \tag{16}$$

[1] For interpretation of color in Figs. 11 and 16, the reader is referred to the web version of this article.

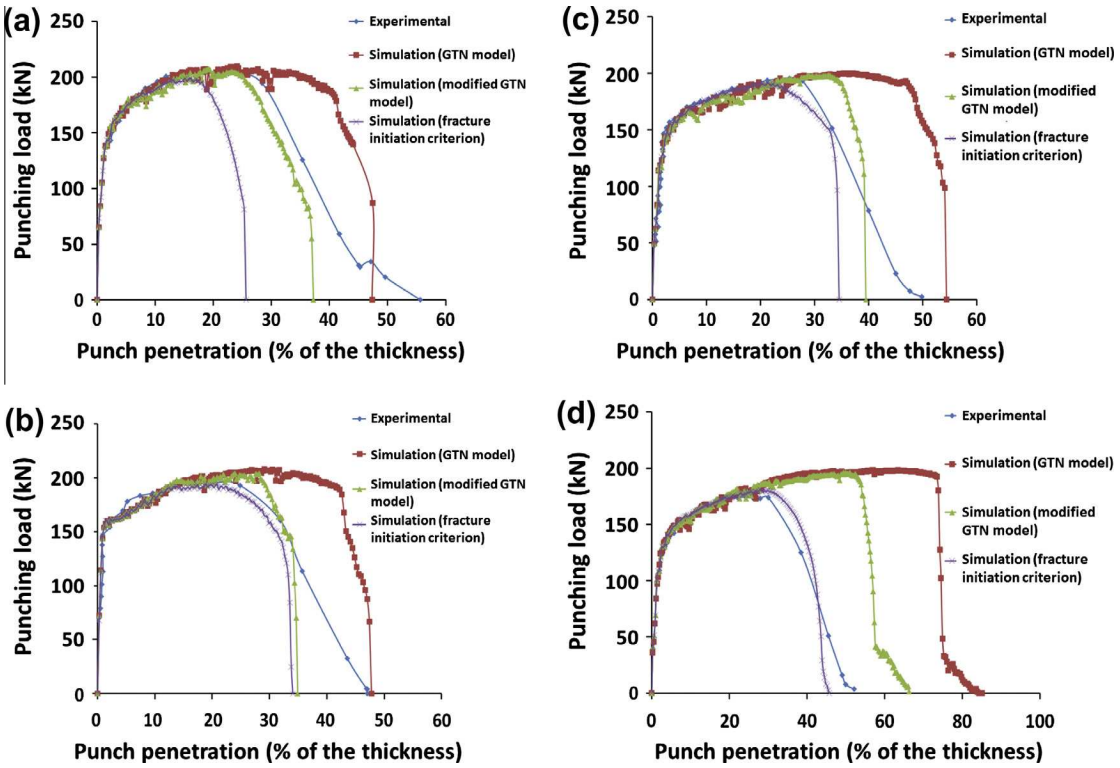

Fig. 12. Prediction of load–penetration curves: (a) $J(\%) = 7$, (b) $J(\%) = 13$, (c) $J(\%) = 17$ and (d) $J(\%) = 31$.

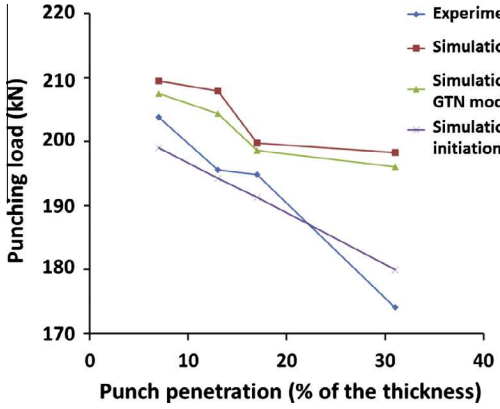

Fig. 13. Effect of clearance variation on the maximum punching load.

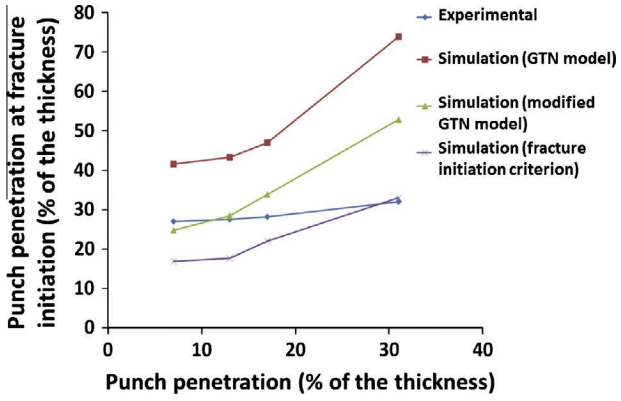

Fig. 14. Effect of clearance variation on the punch penetration at fracture initiation.

where $K_{press} = 31$ KN/mm. This value is determined by minimizing the squared error between the experimental and numerical loads for values varying within the elastic range of the material (0–120 kN). Fig. 11 shows an example of a load–penetration curve, corrected using this method.

4.2.2. Prediction of load–penetration curves

Several numerical simulations have been performed, with the different clearance values tested experimentally, in order to study the influence of the clearance and to validate the fracture models investigated in this study. This is done by comparing the predicted maximum punching load and the penetration associated with fracture initiation, with the experimentally determined values. Fig. 12 shows a comparison between the experimental load–penetration curves and those predicted by the classical GTN model, the modified GTN model and the fracture initiation criterion. These results are analyzed in detail in the following section.

Table 3
Prediction errors (%) for the penetration at fracture initiation.

Clearance (%)	7	13	17	31
Classical GTN model	54,07	57,45	66,66	131,25
Modified GTN model	8,51	3,27	19,85	65,31
Fracture initiation criterion	37,10	35,63	21,98	3,12

4.3. The influence of the punch–die clearance

The punch–die clearance is a process parameter that has a strong influence on the quality of the components produced by punching.

4.3.1. Influence of the punch–die clearance on the maximum load

Fig. 13 shows the evolution of the maximum load versus the punch–die clearance for both the experimental and numerical

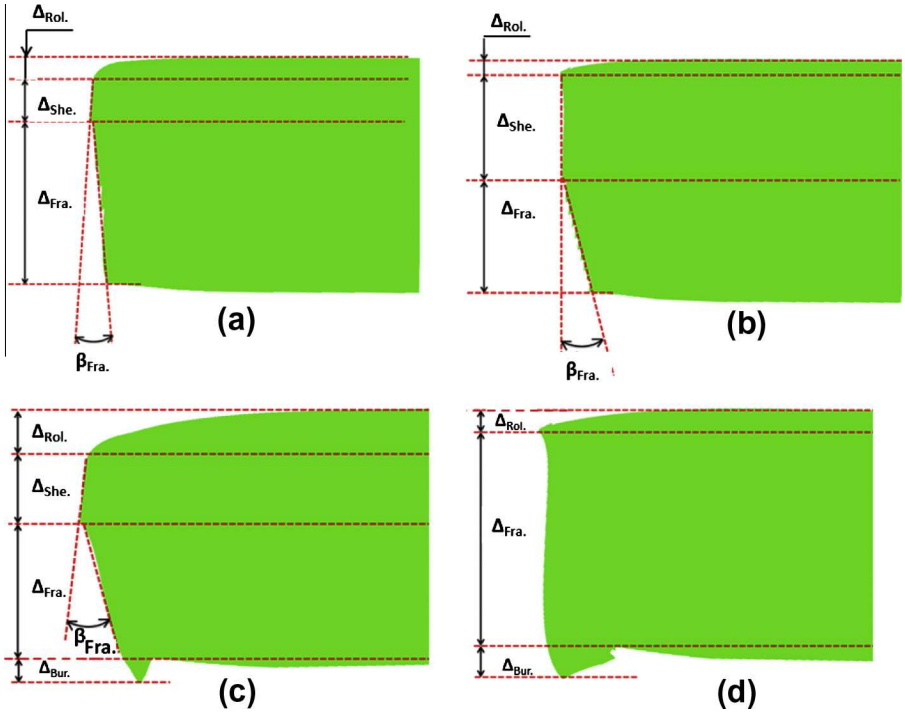

Fig. 15. Examples of numerical profiles after fracture by punching: (a) $J(\%) = 13$ (modified GTN model), (b) $J(\%) = 13$ (fracture ignition criterion), (c) $J(\%) = 31$ (modified GTN model) and (d) $J(\%) = 31$ (fracture initiation criterion).

results. It can be observed that there is a decrease in the maximum punching load when the clearance is increased (i.e. a 204 kN for $J(\%) = 7$ to 174 kN for $J(\%) = 31$). The numerical curves have a similar shape to the experimental curves, for all clearance values. It is observed that the fracture initiation criterion provides an acceptable overall prediction of the maximum load compared to the other damage models. The prediction by the modified GTN model is an improvement compared to the conventional GTN model.

4.3.2. Influence of the clearance on the penetration associated with fracture initiation

The penetration value U_f associated with fracture initiation is calculated by the following formula [35]:

$$U_f = \Delta_{rol.} + \Delta_{she.} + r_p \tag{17}$$

where r_p is the radius of the cutting edge of the punch.

Fig. 14 shows an increase in the value of U_r as a function of the clearance (i.e. 27% of the thickness for $J(\%) = 7$ to 32% of the thickness for $J(\%) = 31$). Table 3 summarizes the prediction errors for the penetration at fracture initiation, with respect to the experimental results. It is noted that the modified GTN model results in good predictions for the penetration at fracture initiation for $J(\%) = 7$ and $J(\%) = 13$, but is less accurate for $J(\%) = 17$ and the prediction for $J(\%) = 31$ is far from the experimental result. This can be explained by the fact that the domain of validity of the parameter k_w of the modified GTN model is limited by the range of stress triaxiality used for its identification. The classical GTN model is unable to predict the correct penetration at fracture initiation for all clearance values. The errors are 54% for $J(\%) = 7$ and approximately 131% for $J(\%) = 31$. This is due to the inadequacy of the model to capture the damage accumulation for shear dominated loads. The prediction errors for fracture initiation criterion decrease with increasing clearance. This criterion gives good predictions for clearances of $J(\%) = 17$ and $J(\%) = 31$, and is less accurate for the other two clearances (7% and 13%).

4.3.3. Influence of the clearance on the evolution of the punched profile zone sizes

Fig. 15 shows some examples of the numerically determined punched profiles obtained after the fracture. Note that the burr zone is absent for a clearance of 13% and that it is present for a clearance 31%. The fracture zone and the fracture angle are absent for the clearance of 31% for the prediction using the fracture initiation criterion. In the last image (Fig. 15d) the existence of two surfaces on the punched zone can be observed (i.e. a concave surface at the top of this area and a convex surface at the bottom before the burr formation).

Fig. 16 shows the evolution of the size of the various zones on the punched profile as a function of the clearance value. For each clearance, the size of the zones shown in Fig. 3 is measured by SEM. Each experimental value is represents an average of five measured specimens.

The rollover zone (Fig. 16a) increases with increasing clearance. This is related to the fact that the sheet is subject to greater bend loads when the clearance is increased. It can be observed that the predicted evolutions of the size of this zone show the same trend, for all of the damage models, as the experimental evolution (i.e. the size of the zone increase with the clearance). The modified GTN model gives good predictions for the size of the rollover area for the first two clearance values, as does the fracture initiation criterion. However, the predictions are less accurate for the two largest clearances.

The sheared zone and the fracture zone (Fig. 16b and c) are the largest surfaces of the punched profile. With increasing clearance, it can be observed experimentally (i.e. the blue curve) that the shear zone decreases and the fracture zone increases. For small clearances, the hydrostatic pressure in the shear zone is the highest which retards the crack initiation necessary to create the fracture zone. These results confirm the results from the literature described in Ref. [11].

The modified GTN model is in good agreement with the experimental results for the first three clearances but is not predictive

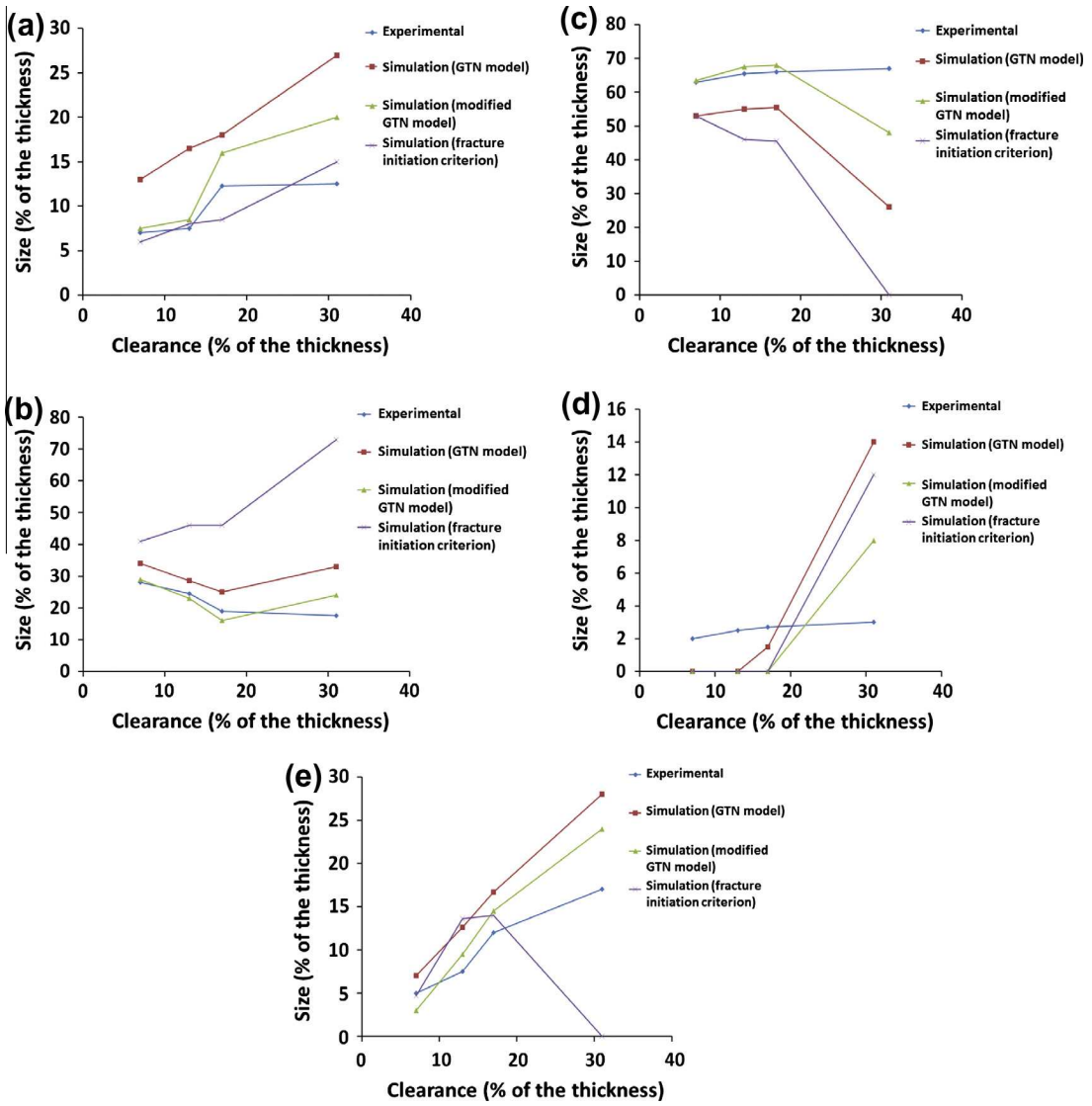

Fig. 16. Evolution of punched profile as a function of the clearance variation: (a) rollover zone, (b) shear zone, (c) fracture zone, (d) burr zone and (e) fracture angle.

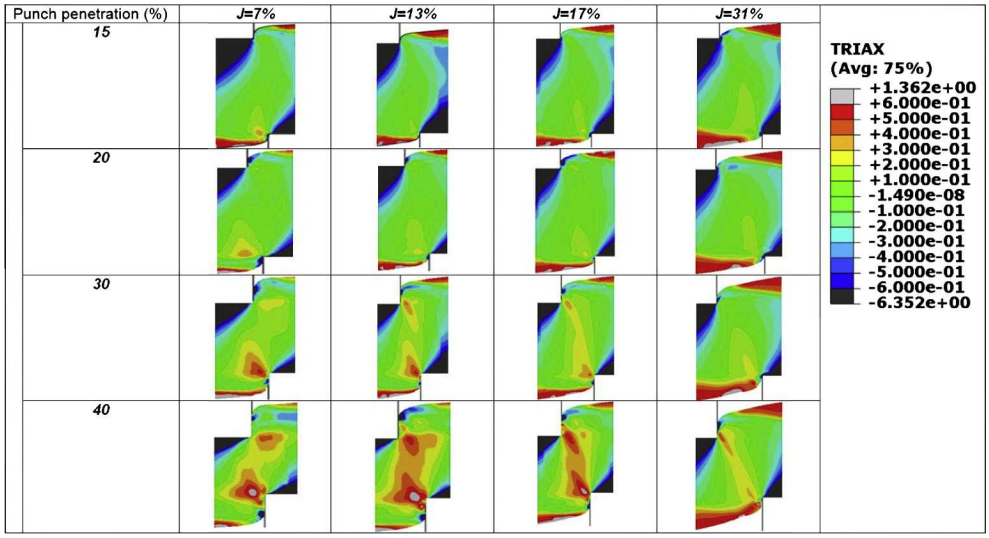

Fig. 17. Evolution of stress triaxiality versus punch penetration for different clearances.

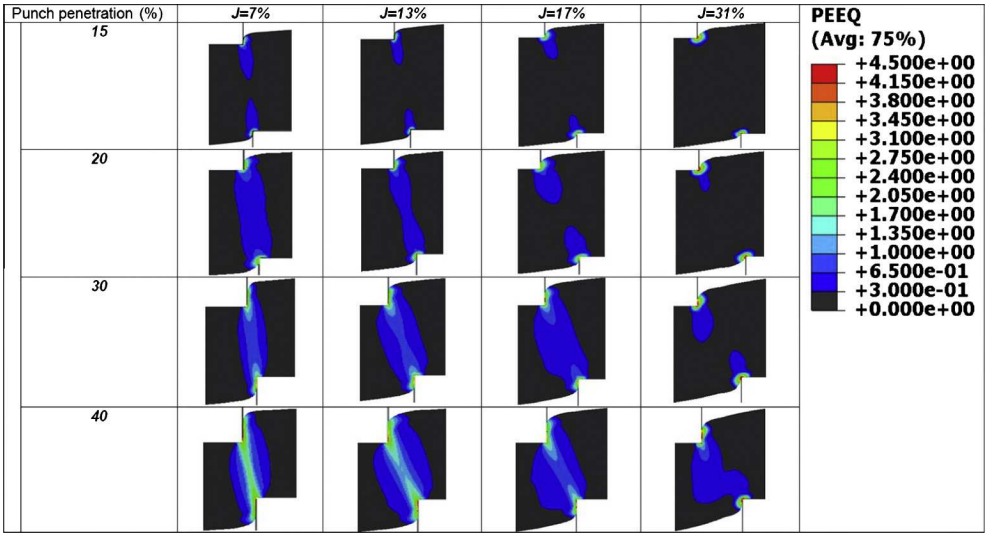

Fig. 18. Evolution of equivalent plastic strain versus punch penetration for different clearances.

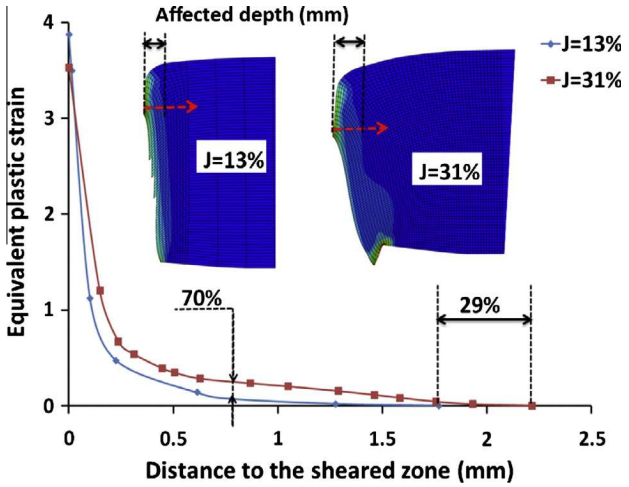

Fig. 19. Evolution of equivalent plastic strain in the most affected region of the shear zone.

for the most important clearance ($J(\%) = 31$) where the evolution is reversed. The prediction of these two parts with the fracture initiation criterion is fairly remote to experimental results.

The evolution of the burr zone, shown in Fig. 16d, shows the increase of this zone with increasing clearance values. The numerical prediction of the size of this area does not correspond to the experimental values. Indeed, the prediction of burr formation is absent for clearances less than 31%. Damaged elements are completely removed for the clearances 7%, 13% and 17%. For a clearance 31%, there is sufficient space for the elements to be deformed more freely and form a burr of significant size.

Fig. 16e shows the evolution of the fracture angle as a function of the clearance for the experimental and numerical results. The experimental curve as well as those predicted by the classical GTN and the modified GTN models show that increasing the clearance leads to a significant increase in the fracture angle and therefore reduces the quality of the punched profile. Note that the numerical prediction obtained by the modified GTN model is in good agreement with the experimental results for the first three clearance values. It is observed that the formation of the fracture angle is absent from the numerical predictions for a clearance of 31% (Figs. 15d and 16e).

4.3.4. Discussion

After having studied the influence of the clearance on (a) the maximum punching load, (b) the penetration at fracture initiation and (c) the evolution of the different zones forming the punched profile, it can be concluded that the choice of a relatively small clearance results in a smoother surface quality by reducing the fracture zone, the fracture angle and burr formation. A small clearance value limits geometrical defects and crack initiation. However, this choice leads to a high stress concentration at the cutting edges of the tools (die and punch) [14], which may result in higher damage and wear and requires greater punching loads. Therefore, an optimal clearance value must be identified on the one hand, to obtain a good surface quality with an acceptable shear zone, and secondly to minimize the stress concentration at the tool cutting edges.

4.4. Prediction of the stress, strain and damage fields

4.4.1. Evolution of stress state

The analysis of the stress state produced in the clearance zone, during the penetration of the punch into the material (Fig. 17), shows that the stress triaxiality varies within a range of −0.2 to 0.6 depending on the level of punch penetration and the clearance value. The normalized third invariant stress remains constant in this zone ($\xi \sim 0$).

For a given value of the clearance, the stress state associated with a punch penetration of 15% is similar to shear mode where the average stress triaxiality in this area does not exceed a value of approximately 0.1. When the punch penetration increases to 20%, the stress state evolves to a state of uniaxial tension. This trend continues up to a punch penetration up about 40% of the thickness of the sheet. The increase in the stress triaxiality is more localized near the cutting edge of the die, and is less pronounced near the cutting edge of the punch. The evolution of the stress triaxiality on both cutting edges, as a function of the punch penetration, results in the formation of a deformation zone that is home to high stresses which promote the initiation and propagation of cracks.

4.4.2. Evolution of the equivalent plastic strain

Fig. 18 shows the distribution of the equivalent plastic strain for various stages of punch penetration and for each clearance value. For each condition, the appearance of a band of localized plastic

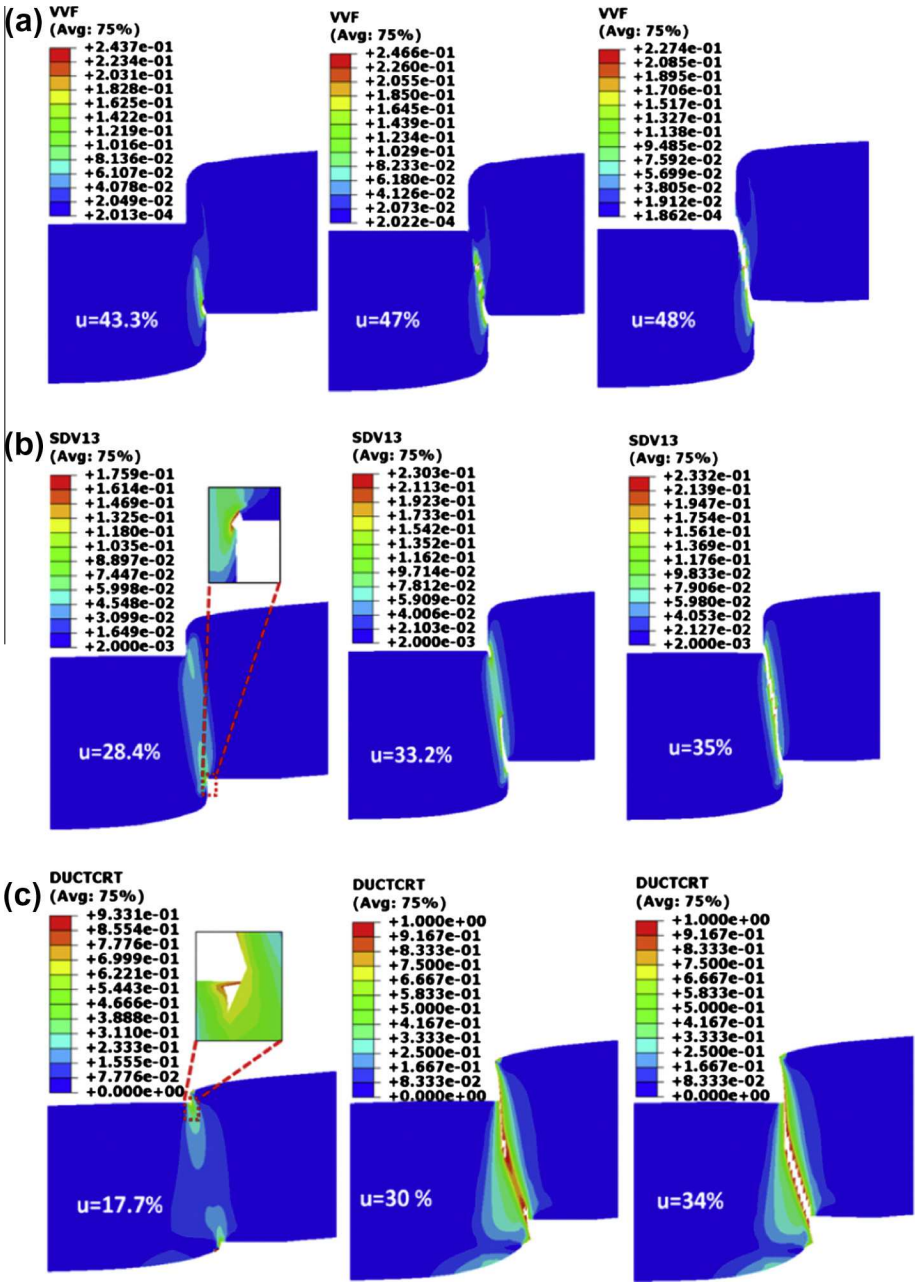

Fig. 20. Damage distribution for different stages of punch penetration ($J(\%) = 13$): (a) classical GTN model; (b) modified GTN model and (c) fracture initiation criterion.

strain can be seen at the contact between the tool cutting edges (punch and die) and the sheet. With increasing punch penetration, this band propagates on both sides, into the thickness of the sheet, to form a zone of plastic strain, the size of which depends on the clearance. The highest values of equivalent plastic strain are obtained for the highest values of punch penetration and smallest clearance value. This region is characterized by a very high level of work hardening prior to the damage phase.

In order to study the impact of the punching process on the punched edge after complete fracture, the hardened zone has been analyzed numerically in terms of its size and degree of hardening. Fig. 19 shows that the equivalent plastic strain decreases from the surface of the punched profile to the center of the heard, which confirms the micro-hardness values shown in Fig. 10. A comparison between the results for two clearance values shows that the clearance affects the hardened depth. That is, an increase in clearance of 13–31% leads to an affected depth, which is 29% larger. The reduction of the clearance results in the high material hardening being localized near the punched profile. The equivalent plastic strain is reduced by 70% at 0.7 mm from the edge. This reduces the probability of cracking.

4.4.3. Damage and fracture predictions

Fig. 20 shows the distribution of the damage parameters (i.e. WF for GTN model, SDV13 for modified GTN model, and DUCTCRT for the fracture initiation criterion) as a function of the punch penetration for the $J(\%) = 13$ condition. As discussed in the previous section, the finite elements models have shown that the plastic strain is localized in the shear zone. During this localization, the displacement of the punch causes damage localization in this area. The damage increases locally to a sufficiently large magnitude to cause internal failure of the material and consequently induce fracture along the thickness.

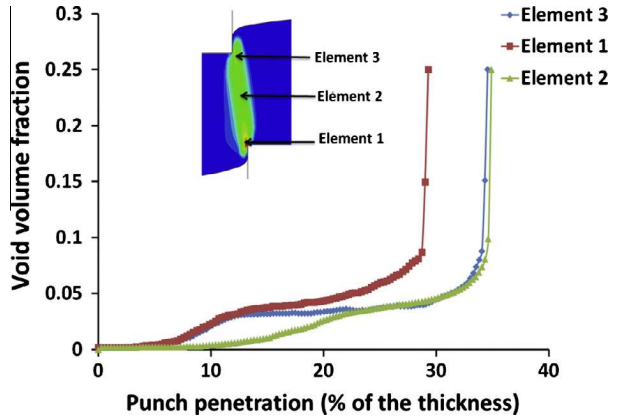

Fig. 21. Evolution of the void volume fraction of three elements in the shear zone obtained by the modified GTN model for $J(\%) = 13$.

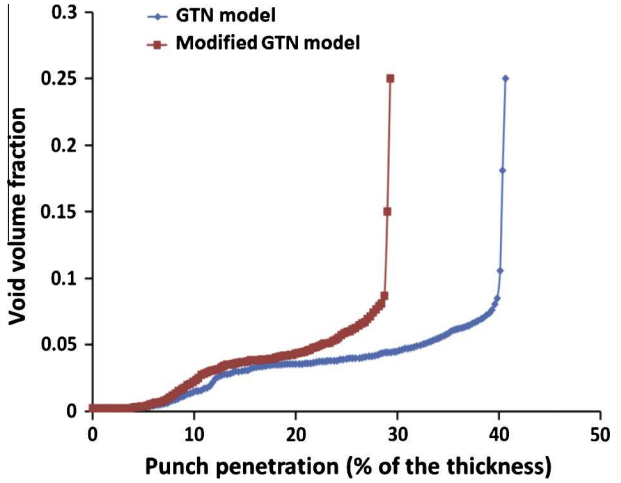

Fig. 22. Evolution of the void volume fraction at fracture initiation for $J(\%) = 13$.

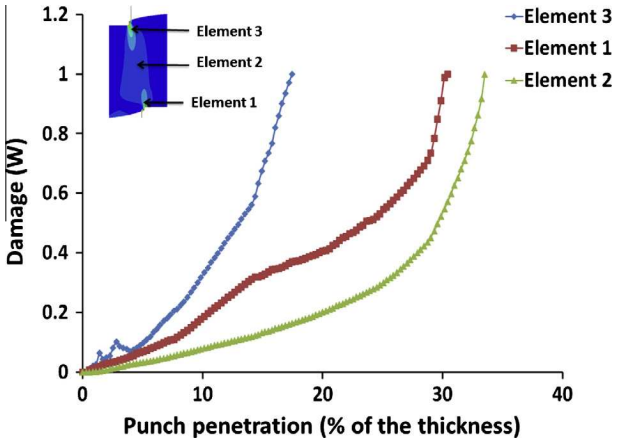

Fig. 23. Evolution of the damage indicator W in three elements of the shear zone obtained by the fracture initiation criterion for $J(\%) = 13$.

The prediction of the location in which crack initiation occurs depends on the used model. Indeed, the classical GTN model, which overestimated the penetration associated with fracture initiation, shows that the crack initiates at the die side cutting edge and propagates in the direction of the contact between the sheet and the punch cutting edge (Fig. 20a).

The predictions obtained by the modified GTN model are shown in Figs. 20b and 21. The damage accumulates and starts to grow at the die cutting edge (at 5% punch penetration) and at the punch cutting edge (at 10% of punch penetration). When the void volume fraction reaches its critical value (8%), fracture initiates at the die side cutting edge at 28.5% punch penetration. It propagates towards another crack created at the punch cutting edge at 33% punch penetration. Both cracks propagate toward the center of the thickness, which leads to total fracture of the material. The numerically predicted fracture location is in good agreement with the experimental observations shown in Fig. 8d.

The evolution of the void volume fraction is more rapid for the modified GTN model when compared to the classical GTN model (Fig. 22). This significant acceleration in the growth rate of the void volume fraction is due to the accumulation of damage induced by the shear term in the modified GTN model which is neglected by the classical GTN model.

Concerning the fracture initiation criterion (Fig. 20c and Fig. 23), the fracture is controlled by the DUCTCRT parameter, which is equivalent to the parameter W in Eq. (12). This parameter increases in the region between the cutting tool edges, due to the increase in plastic strain in this zone (Fig. 18), when the punch penetrates the material. The highest values are observed in the vicinity of the cutting edges of the tools. For a punch penetration of 17.7% of the thickness, the indicator W reaches its maximum value of $W = 1$ near the cutting edge of the punch, causing fracture in this location. This is in contradiction with the experimental observations. At 30% punch penetration, a crack appears in the side of the cutting edge of the die. The fracture process develops on both sides until complete fracture at 34% of punch penetration (Fig. 20 IV).

5. Conclusions

Experimental and numerical investigations of the axisymmetric punching process were conducted in this work and lead to the following conclusions:

- Concerning the microscopic observations for a clearance value of $J(\%) = 13$:
  - The formation of a deformation zone in the clearance zone between the punch and the die is characterized by the complete plastic behavior of the material in this band.
  - The damage is located near the die cutting edge, where crack initiation and propagation occurs.
  - The mechanisms of crack propagation are defined by the interaction between the cavities and/or micro-cracks. These mechanisms locally affect the crack path.
- The plastic strain and the degree of work hardening decrease with the distance from the punched edge to the heard of the part.
- Increasing the clearance between the punch and die results:
  - An increase in the width of the hardened zone on the punched edge.
  - A decrease in the size of shear zone and an increase in the size of the fracture zone and the fracture angle. This favors the presence of geometrical defects and the risk of crack initiation.
  - A decrease in the stress concentration at the cutting edge of the tools, and therefore improves their operational lives.
  - The variation of the plastic strain field and the stress triaxiality in the shear zone.
- The predictions obtained by the modified GTN model, show good agreement with the experimental results when compared to the classical GTN model for clearances in the range of (7–13%). For the clearance range of (13–17%) the predictions are less accurate. For $J(\%) = 31$ the predictions are far from the experimental results.

- The fracture initiation criterion results in good predictions for the maximum punching load and the punch penetration at fracture initiation, for clearances in the range of (17–31%). The predictions of punched profile using this criterion do not correspond well with the experimental observations.
- The fracture angle, which is a function of the clearance, affects the crack propagation path.

References

[1] Hambli R, Potiron A. Finite element modeling of sheet-metal blanking operations with experimental verification. J Mater Process Technol 2000;102:257–65.
[2] Lemiale V, Chambert J, Picart P. Description of numerical techniques with the aim of predicting the sheet metal blanking process by FEM simulation. J Mater Process Technol 2009;209:2723–34.
[3] Cockroft M, Latham D. Ductility and workability of metals. J Inst Met 1968;96:33–9.
[4] Rice J, Tracey D. On the ductile enlargement of voids in triaxial stress fields. J Mech Phys Solids 1969;17:201–17.
[5] Oyane M, Sato T, Okimato K, Shima S. Criteria for ductile fracture and their application. J Mater Process Technol 1980;4:65–81.
[6] Fang G, Zeng P, Lou L. Finite element simulation of the effect of clearance on the forming quality in the blanking process. J Mater Process Technol 2002;122:249–54.
[7] Ko D, Kim B, Choi J. Finite element simulation of the shear process using the element-kill method. J Mater Process Technol 1997;72:129–40.
[8] Kwak T, Kim Y, Bae W. Finite element analysis on the effect of the die clearance on shear planes in fine blanking. J Mater Process Technol 2002;56:462–8.
[9] Hatanaka N, Yamaguchi K, Takakura N. Finite element simulation of the shearing mechanism in the blanking of sheet metal. J Mater Process Technol 2003;139:64–70.
[10] Bacha A, Daniel D, Klocker H. Crack deviation during trimming of aluminium automotive sheets. J Mater Process Technol 2010;210:1885–97.
[11] Goijaerts A, Govaert LE, Baaijens F. Evaluation of ductile fracture models for the different metals in blanking. J Mater Process Technol 2001;110:312–23.
[12] Shim K, Lee S, Kang B, Hwang S. Investigation on blanking of thin sheet metal using the ductile fracture criterion and its experimental verification. J Mater Process Technol 2004;155:1935–42.
[13] Mediavilla J, Peerlings R, Geers M. An integrated continuous discontinuous approach towards damage engineering in sheet metal forming processes. Eng Fract Mech 2006;73:895–916.
[14] Farzin M, Javani H, Mashayekhi M, Hambli R. Analysis of blanking process using various damage criteria. J Mater Process Technol 2006;177:287–90.
[15] Hambli R, Reszka M. Fracture criteria identification using an inverse technique method in blanking experiment. Int J Mech Sci 2002;44:1349–61.
[16] Thipprakmasa S, Jin M, Tomokazuc K, Katsuhiroc Y, Murakawab M. Prediction of Fine blanked surface characteristics using the finite element method (FEM). J Mater Process Technol 2008;198:391–8.
[17] Lemaitre J. A continuous damage mechanics model for ductile fracture. J Eng Mater Technol 1985;107:83–9.
[18] Gurson AL. Continuum theory of ductile rupture by void nucleation and growth: Part I – Yield criteria and flow rules for porous ductile media. J Eng Math Tech, Trans ASME 1977;9:2–15.
[19] Tvergaard V, Needleman A. Analysis of the cup-cone fracture in a round tensile bar. Acta Metall Mater 1984;32:157–69.
[20] Nahshon K, Hutchinson J. Modification of the Gurson model for shear failure. Eur J Mech A/Solids 2008;27:1–17.
[21] Nielsen K, Tvergaard V. Ductile shear failure or plug failure of spot welds modelled by modified Gurson model. Eng Fract Mech 2010;77:1031–47.
[22] Hibbitt, Karlsson, Sorensen. ABAQUS User's Manual 2010. Version 6.10.
[23] Husson C, Correia J, Daridon L, Ahzi S. Finite elements simulations of thin copper sheets blanking: study of blanking parameters on sheared edge quality. J Mater Process Technol 2008;199:74–83.
[24] Chu C, Needleman A. Void nucleation effects in biaxially stretched sheets. J Eng Mater Technol 1980;102(3):249–56.
[25] Achouri M, Germain G, Dal Santo P, Saidane D. Experimental characterization and numerical modeling of micromechanical damage under different stress states. Mater Des 2013;50:207–22.
[26] Achouri M, Germain G, Dal Santo P, Saidane D. Numerical integration of an advanced Gurson model for shear loading: application to the blanking process. Comput Mater Sci 2013;72:62–7.
[27] Kut S. The application of the formability utilization indicator for finite element modeling the ductile fracture during the material blanking process. Mater Des 2010;31:3244–52.
[28] Gao X, Zhang G, Roe C. A study on the effect of the stress state on ductile fracture. Int J Damage Mech 2009;19:75–94.
[29] Bai Y, Wierzbicki T. A new model of metal plasticity and fracture with pressure and lode dependence. Int J Plast 2008;24:1071–96.
[30] Brünig M, Chyra O, Albrecht D, Driemeier L, Alves M. A ductile damage criterion at various stress triaxialities. Int J Plast 2008;24:1731–55.
[31] Dunand M, Mohr D. On the predictive capabilities of the shear modified Gurson and the modified Mohr–Coulomb fracture models over a wide range of stress triaxialities and Lode angles. J Mech Phys Solids 2011;59:1374–94.
[32] Broberg K. Crack growth criteria and non-linear fracture mechanics. J Mech Phys Solids 1971;19:407–18.
[33] Stegeman Y, Goijaerts A, Brokken D, Brekelmans W, Govaert L, Baaijens F. An experimental and numerical study of a planar blanking process. J Mater Process Technol 1999;87:266–76.
[34] Gram M, Wagoner R. Fine blanking of high strength steels: control of material properties for tool life. J Mater Process Technol 2011;211:717–28.
[35] Bacha A, Daniel D, Klocker H. Crack deviation during trimming of aluminum automotive sheets. J Mater Process Technol 2010;210:1885–97.